encit 2020

ABCM Associação Brasileira de Engenharia e Ciências Mecânicas

18th Brazilian Congress of Thermal Sciences and Engineering
November 16–20, 2020 (Online)

ENCIT 2020-0742
Numerical Analysis Of The Water Vapour Through The Feed System Of The Low-Pressure Micro-Resistojet

Igor Pimentel Guimarães
Daduí Cordeiro Guerrieri
Mechanical Engineering Department, CEFET-RJ Campus Itaguaí, Rio de Janeiro, Brazil
igor.guimaraes@aluno.cefet-rj.br, dadui.guerrieri@cefet-rj.br

Abstract. *Cubesats have changed the paradigm of nanosatellites and have demonstrated several possibilities for technological innovation. The space industry has seen an increase in the number of nanosatellites launched lately. However, due to strict safety requirements or mission types, only* $5\,\%$ *were launched containing propulsion systems. The Low-Pressure Micro-Resistojet (LPM) uses electrical power to heat a gas through the heater chip, transforming enthalpy into kinetic energy generating thrust. The main aspect of this thruster type is that it works under very low pressure, being able to generate low thrust levels and ensuring a wider range of propulsive force. Additionally, the use of water as a green propellant has been proved a promising alternative to overcome many safety issues imposed without losing performance. Therefore, this paper describes a numerical analysis of the feed system and plenum for a Low-Pressure Micro-Resistojet working with water vapor at sublimation conditions inside the tube. The OpenFOAM software was used to simulate the flow behavior under different boundary conditions. It is shown that the LPM can generate different levels of thrust by properly controlling the phase change condition.*

Keywords: *Micro-Resistojet, green propellant, low-pressure, feed system, nanosatellite*

1. INTRODUCTION

Cubesats started as a project to provide affordable space access for the university science community and suddenly became a trend towards standardization of nanosatellites, used not only by major universities, but also high school, middle school, elementary school, government agencies, educational institutions and commercial groups around the world. A Cubesat unit, consists of a $10\,\mathrm{cm}$ cube with mass ranging from $1\,\mathrm{kg}$ to $1.33\,\mathrm{kg}$ (CGEE, 2004; NASA, 2017; Mehrparvar *et al.*, 2014). The first Cubesats were launched in 2003, proving all their technological and commercial potential. It was then realized that small standardized structures could reduce the costs, the development time, and even the risk involved since it allows a usual complex mission to be divided into small missions containing individual Cubesats. Throughout the past decade, Cubesats were the main type of nanosatellites used, and the reducing costs of Cubesats missions is becoming more feasible due to the fast technology advancements in microelectronics, coupled with the intense use of commercial of-the-shelf (COTS) components in Cubesats (Villela *et al.*, 2019).

Despite the recent increase in space missions involving Cubesats, only $5\,\%$ were launched containing propulsion systems (Kulu, 2020). Thrusters have proven to be essential when combined with Cubesats, as they increase their useful life, reduce costs, improve their applicability and enable new horizons of movements such as orbital maneuvers, drag compensation and re-entry control (Silva *et al.*, 2018; Guerrieri, 2018a). In addition, they make possible new missions types such as formation flight to provide 5G internet and constellation of Cubesats in high orbit for formation of virtual telescope (Bassoli *et al.*, 2020; Naseri *et al.*, 2018).

Resistojets are electrothermal propulsion systems that use electrical power to heat a gas through a heater. The heated propellant gas is then accelerated through the nozzle, transforming enthalpy into kinetic energy generating thrust (Lemmer, 2017; Storck *et al.*, 2006). The Low-Pressure Micro-Resistojet (LPM) is a type of Microelectromechanical systems (MEMS) that operates at very low levels of pressure, in the order of $10^2\,\mathrm{Pa}$. The LPM is characterized by rarefied gas dynamics principles with the thruster part under the free-molecule regime (Guerrieri *et al.*, 2018b). However, other parts of the device are under different flow regime, depending on its properties and characteristic dimensions. The flow dynamics in the proposed feeding system is defined as slip flow regime. The Navier-Stokes equations are applied considering the water vapor as a compressible flow. Thus, the free software OpenFOAM is used to solve the governing equations using the Finite Volume Method. With that, it is possible to describe the phenomena and their inherent peculiarities for different boundary conditions.

2. PROPULSION CONCEPT

The LPM can be simplified into three main parts, the propellant storage tank, feed system and thruster, as shown in Fig. 1. Low pressures allow the propellant to be stored in both solid and liquid states, and a heater is generally used to generate phase change. The feed system is usually composed of tubes and valves connecting the tank to plenum. The thruster part can be divided into two parts, plenum and the heater chip. The water vapor, after leaving the feed system, passes through the plenum and then goes to the microchannels of the heater chip, being then expelled into space, generating thrust (Guerrieri *et al.*, 2018c).

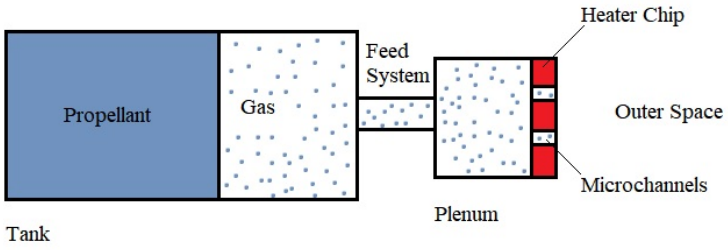

Figure 1. The scheme of the LPM is composed of a tank, feed system, and thruster.

The LPM presents several advantages for nanosatellites, as they work at low pressure, which makes the system lighter and more reliable. Another beneficial feature is that they can act in any power range, including Cold Gas conditions. Additionally, lower pressures help reduce leakage issues, therefore, it will make it more feasible to fit into strict mission requirements (Lee *et al.*, 2008; Guerrieri *et al.*, 2018b).

It has been shown by (Guerrieri *et al.*, 2017), that out of the 95 fluids listed, water is the most promising one, it is a green propellant, the safest one, the more abundant, the cheapest, and also has the best velocity increment per volume of propellant. For typical nanosatellites missions, it can be stored in liquid or solid phase. In addition, water can overcome the strict requirements for space missions, and is a very promising resource for future deep space exploration (Asakawa *et al.*, 2019).

3. THEORETICAL AND NUMERICAL MODELING

In the present work, the tube is considered both as propellant storage tank and as a feeding system as suggested by (Guerrieri *et al.*, 2018b). The propellant works under sublimation conditions, which means that pressure and temperature must be below the water triple point of $611\,\mathrm{Pa}$ and $273\,\mathrm{K}$, respectively, to avoid liquid phase. Only the phase change from ice to vapor is considered, meaning that pressure and temperature in the tank shall follow the sublimation curve in Eq. 1 (Wagner *et al.*, 1994).

$$\ln \frac{P_s}{P_t} = a(1-\theta^{-1.5}) + b(1-\theta^{-1.25}) \tag{1}$$

where P_s is the sublimation pressure, P_t the pressure for triple point of water, equals to $611.657\,\mathrm{Pa}$, a a coefficient equals to -13.9281690, b a coefficient equals to 34.7078238, and $\theta = \frac{T_s}{T_t}$ where Ts is the sublimation temperature, and Tt is the triple point temperature of water equals to $273.16\,\mathrm{K}$. Equation 1 is only valid for temperatures between $190\,\mathrm{K}$ and $273.16\,\mathrm{K}$.

Resistojets operates under different flow regime through different parts of its system, going from continuum flow regime at the tank do free molecular flow regime at outer space, Tab. 1. To define the flow regime, it is used the Knudsen number (Kn), a dimensionless number, that describes the degrees of rarefaction of the gas using the equation

$$Kn = \frac{\lambda}{D} \tag{2}$$

where, λ is the mean free path, and D the characteristic length scale.

Table 1. Different gas regimes. Data rearranged from (Karniadakis *et al.*, 2006)

Knudsen Number	regime
$Kn \approx 0$	Inviscid flow
$Kn \leqslant 0.001$	Continuum regime
$0.001 \leqslant Kn \leqslant 0.1$	Slip regime
$0.1 \leqslant Kn \leqslant 10$	Transition regime
$Kn \geq 10$	Free-molecular regime

In this work, the flow from the feed system to the plenum is modeled under the Slip flow regime, with Knudsen number ranging from 0.0034 to 0.0453. The water vapor is considered an ideal gas. The Computational fluid dynamics (*CFD*) software, OpenFOAM is applied. OpenFOAM is a free open source C++ library to create applications for fluid and solid simulations (Greenshields, 2015). One of the many solvers for fluids in OpenFOAM is the *rhoCentralFoam*, which is a density-based compressible flow solver that uses semi-discrete, non-staggered central schemes (Greenshields *et al.*, 2010). The *rhoCentralFoam* solves each of the governing equations separately. First, the continuity is applied, to obtain density using the velocity from the last time setp (Trydal, 2015)

$$\frac{\partial \rho}{\partial t} + div(\rho \mathbf{u}) \; = \; 0 \tag{3}$$

where, ρ is the density and $\boldsymbol{u}$ the flow velocity. Then the momentum equation is solved in two steps to avoid explicit solution. The inviscid momentum density, $\widehat{\boldsymbol{u}}$, is calculated as

$$\left(\frac{\partial \widehat{\mathbf{u}}}{\partial t}\right)_I + div(u\widehat{\mathbf{u}}) + div\, p \; = \; 0 \tag{4}$$

where $\left(\frac{\partial \widehat{\boldsymbol{u}}}{\partial t}\right)_I$ is the time derivative due to inviscid fluxes only, and $\widehat{\boldsymbol{u}} \; = \; \rho \boldsymbol{u}$. Next, the viscous forces are included by solving a diffusion correction equation for $\boldsymbol{u}$ through

$$\left(\frac{\partial (\rho \mathbf{u})}{\partial t}\right)_V - div(\mu \, grad(\mathbf{u})) - div\, \mathbf{T}_{visc} \; = \; 0 \tag{5}$$

where $\left(\frac{\partial (\rho \boldsymbol{u})}{\partial t}\right)_V$ is the time derivative related to diffusion only, $\boldsymbol{T}_{visc}$ the viscous stress tensor and μ the dynamic viscosity of the fluid. The energy equation is applied using the same approach. First, it is solved for the total energy density, $\widehat{E}$, neglecting the diffusive heat flux

$$\left(\frac{\partial \widehat{E}}{\partial t}\right)_I + div(\mathbf{u}\,(\widehat{E} + \rho)) + div\; T.\mathbf{u} \; = \; 0 \tag{6}$$

where $\widehat{E} \; = \; \rho E$. The temperature is calculated as

$$T \; = \; \frac{1}{c_v}\left(\frac{\widehat{E}}{\rho} - \frac{|\mathbf{u}|^2}{2}\right) \tag{7}$$

where c_v is the specific heat capacity at constant volume. Then the diffusive heat flux is included through the following equation

$$\left(\frac{\partial (\rho \, c_v \, T))}{\partial t}\right)_V \; - \; div(k_c \; grad(T)) \; = \; 0 \tag{8}$$

where k_c is the thermal conductivity. Finally, the pressure is updated by the final step of each interaction through the ideal gas law

$$p \; = \; \rho \, R T \tag{9}$$

where *R* is the universal gas constant.

The mesh showed in Fig. 2 was built within the *OpenFOAM* using the *blockMesh* command to generate the mesh. In this paper, the tube and the plenum are represented as two concentric cylinders, the tube with a $0.8\,\mathrm{mm}$ diameter and the plenum with a $12\,\mathrm{mm}$ diameter. To reduce the simulation time, it was used the axis-symmetric modeling representing just a wedge, see Fig. 2.

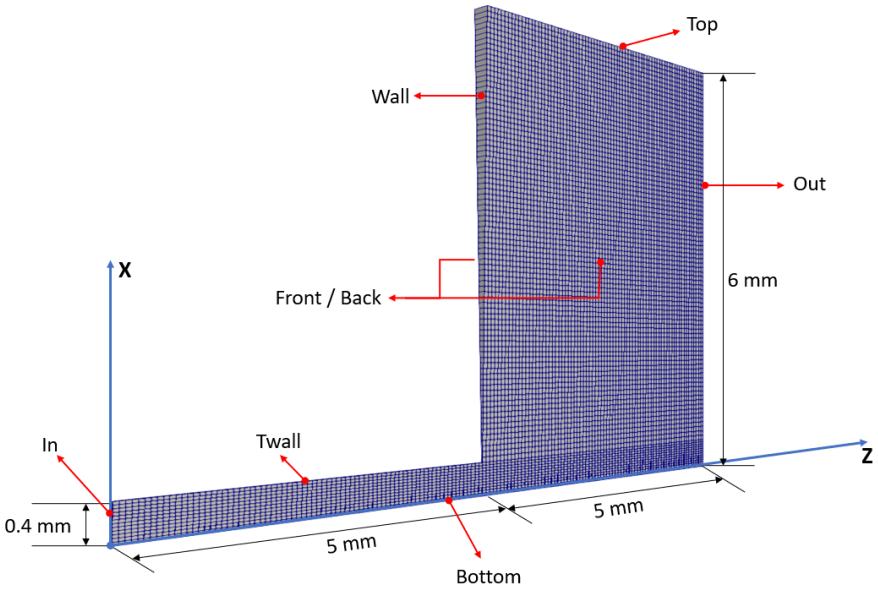

Figure 2. The mesh and boundary conditions scheme of the wedge that model the feed system and plenum.

A mesh sensitive analysis was performed in order to assess the difference in the results obtained for different number of cells and different time step. Five meshes were used with 900 cells, 3600 cells, 8100 cells, 14400 cells and 22500 cells using the same boundary conditions of *case 1*, Tab. 2, with a fixed time step of $1 \times 10^{-8}\,\mathrm{s}$, simulated up to $1 \times 10^{-2}\,\mathrm{s}$. Five time steps were tested with $2 \times 10^{-9}\,\mathrm{s}$, $5 \times 10^{-9}\,\mathrm{s}$, $1 \times 10^{-8}\,\mathrm{s}$, $2 \times 10^{-8}\,\mathrm{s}$ and $3 \times 10^{-8}\,\mathrm{s}$ using the same boundary conditions previously mentioned, using the 8100 cells mesh as reference, simulated up to $1 \times 10^{-3}\,\mathrm{s}$ to minimize the computational effort. The results obtained for mass flow, speed, temperature and density represent an average at the outlet face area, and they were used to evaluate the different meshes and time steps.

The simulated cases presented in Tab. 2 were solved using the *rhoCentralFoam* for a ideal gas, laminar flow and compressible flow. The inlet is considered to work below the water triple, with $600\,\mathrm{Pa}$ as the maximum acceptable pressure. The inlet temperature can be obtained with the respective pressure through Eq. 1. An ambient temperature of $300\,\mathrm{K}$ was set based on the maximum and minimum operational temperatures of different components inside a Cubesat (Kang and Oh, 2016). The plenum pressure (P_0) is set at a maximum of $300\,\mathrm{K}$ for working operation of the plenum and microchannel at the transition or free-molecule regime. The *endTime* was set to make sure the steady-state is obtained.

Table 2. Simulated Cases

	Case 1	Case 2	Case 3	Case 4	Case 5	Case 6	Case 7	Case 8
P_s (Pa)	600	600	600	450	450	450	300	300
P_0 (Pa)	300	150	50	300	150	50	150	50
T_s (K)	272.9271	272.9271	272.9271	269.4840	269.4840	269.4840	264.7766	264.7766
T_{walls} (K)	300	300	300	300	300	300	300	300
endTime (s)	1×10^{-2}	1×10^{-2}	1×10^{-2}	1×10^{-2}	1×10^{-2}	1×10^{-2}	1×10^{-2}	1×10^{-2}
Δt (s)	1×10^{-8}	1×10^{-8}	5×10^{-9}	1×10^{-8}	1×10^{-8}	1×10^{-8}	1×10^{-8}	1×10^{-8}

The solver *rhoCentralFoam* requires three boundary conditions at the initial time step, described in Tab. 3. The *internalField* initialize the center points of each individual cell. The *in* and *out* face has fixed values of pressure described accordingly to differents case set up, Tab. 2. The wedge patch is used to reduce computational effort, analyzing only a slice of the total geometry. In *OpenFOAM* it is possible to create wedges with 5° or lower (Greenshields, 2015). The *in*

patch has fixed temperature defined according to the *in* pressure through Eq. 1. The slip condition is applied at *Twalls* in order to better fit Navier-Stokes equations for the slip flow regime.

Table 3. Boundary conditions

Patch	Pressure (Pa)	Temperature (K)	Velocity (m/s)
internalField	300	T_s	(0 0 0)
in	P_s	T_s	zeroGradient
out	P_0	zeroGradient	zeroGradient
Twall	zeroGradient	300	slip
wall	zeroGradient	300	(0 0 0)
top	zeroGradient	300	(0 0 0)
bottom	empty	empty	empty
front	wedge	wedge	wedge
back	wedge	wedge	wedge

4. RESULTS AND DISCUSSION

A mesh sensitivity analysis was carried out using five different meshes with the same boundary conditions, simulated until the steady state was achieved. Table 4 presents the mean velocity (U_0) and mass flow ($\dot{m}_0$), over the *out* face. The 8100 cells mesh presents a minimum Δx of $33\,\mu\mathrm{m}$, maximum Δx of $66\,\mu\mathrm{m}$ and it was chosen because it has a simulation time about 2 times faster and presents results with differences of less than $0.07\,\%$ than the more refined mesh with 22500 cells. For the time step (Δt) sensitivity analysis was performed in order to choose the better trade off between computational effort, convergence and obtained results, therefore five different time steps were tested, Tab. 4. Shorter time steps show less residual error between iterations, meanwhile, it takes more time to simulate the whole case. The Δt of $1 \times 10^{-8}\,\mathrm{s}$ was almost five times faster than the Δt of $1 \times 10^{-9}\,\mathrm{s}$, showed percentage differences below $0.06\,\%$. Therefore, it was the chosen time step for all the simulations performed, with exception of *case 3*, Tab. 2, which required a more refined time step.

Table 4. Comparison between results obtained with different parameters

Parameters		U_0 (m/s)	Difference (%)	$\dot{m}_0$ (kg/s)	Difference (%)	Execution Time
Cells	900	2.93535	3.21	$4.000\,50 \times 10^{-9}$	3.13	5 h 41 min
	3600	2.85855	0.51	$3.898\,40 \times 10^{-9}$	0.50	7 h 41 min
	8100	2.84414	—	$3.879\,15 \times 10^{-9}$	—	19 h 4 min
	14400	2.84211	0.07	$3.876\,48 \times 10^{-9}$	0.07	20 h 24 min
	22500	2.84549	0.05	$3.881\,18 \times 10^{-9}$	0.05	34 h 28 min
Δt (s)	$\Delta t\ 2 \times 10^{-9}$	2.91739	0.06	$4.079\,97 \times 10^{-9}$	0.06	9 h 23 min
	$\Delta t\ 5 \times 10^{-9}$	2.91664	0.04	$4.078\,93 \times 10^{-9}$	0.04	4 h 33 min
	$\Delta t\ 1 \times 10^{-8}$	2.91557	—	$4.077\,48 \times 10^{-9}$	—	2 h 1 min
	$\Delta t\ 2 \times 10^{-8}$	2.91308	0.09	$4.074\,15 \times 10^{-9}$	0.08	1 h 15 min
	$\Delta t\ 3 \times 10^{-8}$	2.90746	0.28	$4.066\,60 \times 10^{-9}$	0.27	0 h 41 min

Once the quality of the mesh and the time step has been ensured, the simulation phase begins for each of the eight cases described at Tab. 2. After the simulations were done, a free post-processing tool, *paraview* (Ahrens *et al.*, 2005), was used to analyze the results. Figure 3 presents different values along the Z axis (center line) from the inlet to outlet. Figure 3(d) is the main legend for the different plots, where the colors are related to the plenum pressure, and the line types are referent to the sublimation pressure.

Figure 3 (a) represents the pressure behavior over the central axis. The pressure decay profile was similar in all cases, across the tube region. The cases with plenum pressure of 50 Pa - *case 3, 6 and 8* -, showed greater pressure drops at the entrance of the plenum, and consequently higher velocities, Fig. 3 (b). Cases with lower differential pressure between tube and plenum showed a more stable profile, showing lower pressure peaks along the axis. The lowest pressure along the center-line was $13\,\mathrm{Pa}$ and occurred in *case 3*.

At Figure 3 (b), we can observe that all cases presented similar inlet velocity ranging from $260\,\mathrm{m\,s^{-1}}$ to $303\,\mathrm{m\,s^{-1}}$, and similar behavior inside the tube. A maximum velocity of $835\,\mathrm{m\,s^{-1}}$ occurred at the *case 3*, that might cause shock waves generating instability at the LPM what is not desirable. The *case 4* presented the more stable velocity profile, with

the lowest high peak of $427\,\mathrm{m\,s^{-1}}$ right after exiting the tube.

The inlet temperature was maintained as a fixed value corresponding to the vapor pressure of each case set up, Tab. 2. Figure 3 (c) describes the temperature along the center-line. All walls are considered to have $300\,\mathrm{K}$ as an ambient temperature, therefore, most of the cases present temperatures lower than $300\,\mathrm{K}$. Similar to pressure, a drop of temperature occurs in all cases, at the plenum entrance, with the lowest value of temperature of $122\,\mathrm{K}$ for the *case 3*. Figure 3 (a) and (b) presents regions with pressure and temperature above the sublimation curve, Eq. 1. Therefore, if enough energy (heat) is removed from the gas, an appearance of solid phase may occur through deposition of water, which is not desirable for LPM that works with gas flow at the plenum.

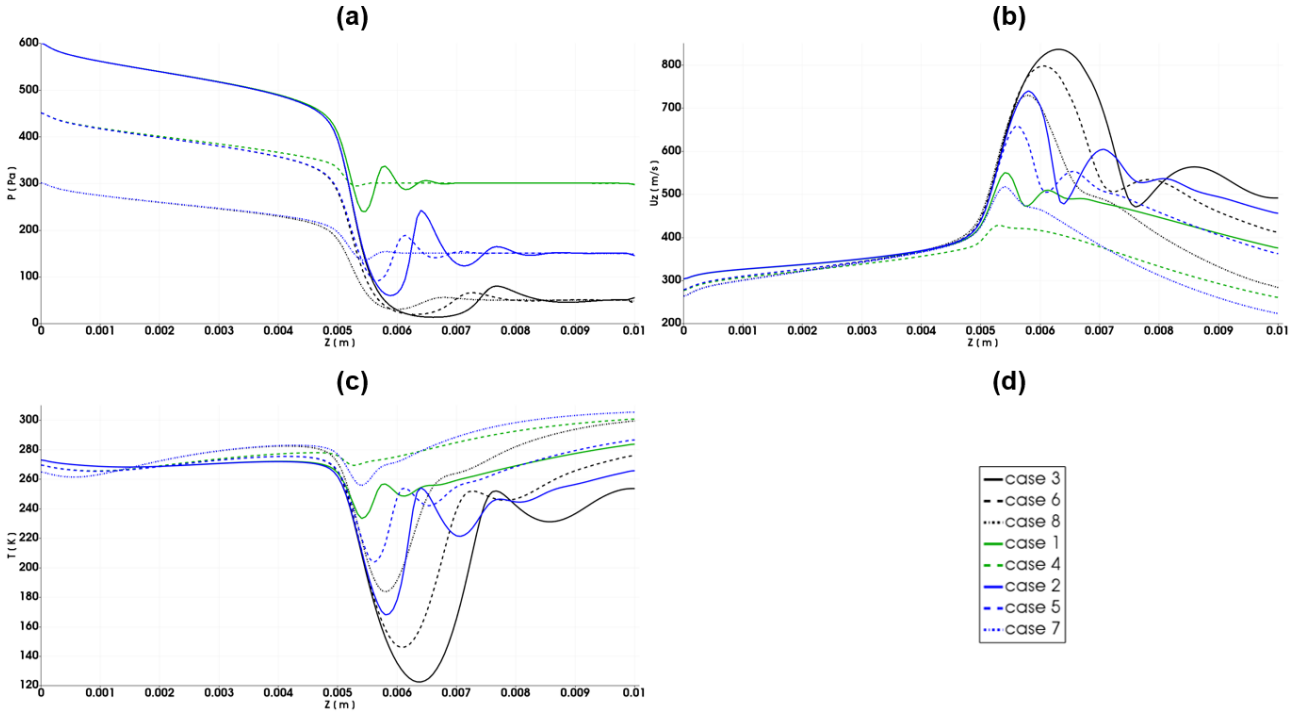

Figure 3. Plot of pressure (a), velocity (b) and temperature (c) along the Z axis (center-line) through the feed system and plenum for all simulated cases. Main legend for all cases testeds (d)

Figure 4 presents the results for $450\,\mathrm{Pa}$ of sublimation pressure and plenum pressure of $300\,\mathrm{Pa}$ (*case 4*). As seen in Figure 3, the pressure decay is more uniform along the domain, for this case set up, Fig. 4 (a). A small region with low pressure occurs at the joint of the tube with the plenum. This may have occurred due to the difference in the boundary condition of the upper tube wall (Twall) with slip condition and the front wall (*wall*) having a zero velocity condition.

With shorter distances from the heated walls, the heat transfer is favored, presenting higher temperatures in relation to more distant points, as seen in Fig. 4 (b). Compared to the other simulated cases, the *case 4* and *7* presented lower variation along the center line of the domain and lower drop of temperature at the entrance of the plenum. This decay can be observed in Fig. 4 (b). A region with higher temperature has occurred at the junction of the tube with plenum. This may have occurred due to the collision between particles in re-circulation with particles heated by the wall and particles coming out of the tube.

The complete velocity map can be seen in Figure 4 (c), with a maximum value of $427.6\,\mathrm{m\,s^{-1}}$ at the plenum entrance. A vorticity effect at the outlet face created a re-circulation zone at thee upper part of plenum, represented by the blue zone in Fig. 4. The speed of sound in the medium of $409\,\mathrm{m\,s^{-1}}$ is estimated using the P_s and the water triple point temperature (Lemmon *et al.*, 2011). Figure 4 (d) shows the map of the mach number along the domain, with a maximum value of approximately 1, describing a transonic flow condition at the first part of the plenum entrance and subsonic speeds throughout the rest of the domain. Having subsonic speeds at the feed system and plenum helps the stability and control of the thruster, avoiding shock waves and disturbances along the system.

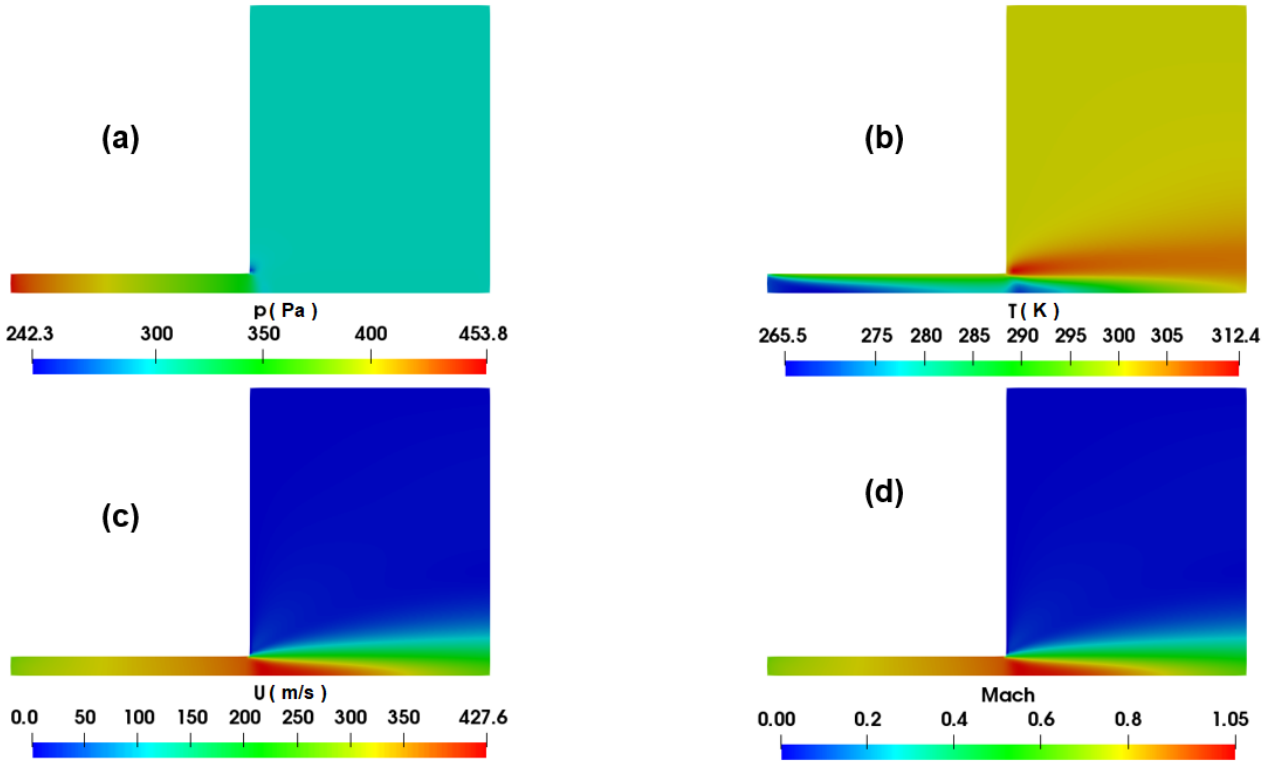

Figure 4. Pressure (a), temperature (b), velocity (c) and Mach number (d) maps throughout the domain for *case 4*

Table 5 presents the mean value of the Pressure, Velocity, Temperature, and density calculated by integration. The mean mass flow rate was calculated to represent the total mass flow rate of the entire plenum, not just the wedge. As the sublimation pressure (P_s) decreases the mass flow rate through the outlet ($\dot{m}_0$) decreases, meaning that the thruster can be controlled with the sublimation variation of the ice, having lower or higher mass flow depending on the feed system pressure. The maximum mass flow value of $6.88 \times 10^{-7}\,\mathrm{kg\,s^{-1}}$ occurred with $600\,\mathrm{Pa}$ of sublimation pressure (P_s), and $300\,\mathrm{Pa}$ (P_0) of plenum pressure. The mean velocity in the plenum (U_0) at the outlet shows to be higher for lower plenum pressure having the maximum velocity for sublimation pressore of $600\,\mathrm{Pa}$ and plenum pressure of $50\,\mathrm{Pa}$. For a good LPM functionality the plenum is desired to have lower velocities, in order to better accommodate the flow speed coming from the feed system , which has a lower cross-section area, to the plenum. The mean temperature at the outlet showed small variations, increasing as the sublimation pressure increases, with a maximum value of $302.491\,\mathrm{K}$. The mean density at outlet (ρ_0) presented small variation according to the sublimation pressure, where higher values of pressure generate higher densities.

Table 5. Results at the outlet face

P_s (Pa)	P_0 (Pa)	U_0 (m/s)	$\dot{m}_0$ (kg/s)	T_0 (K)	ρ_0 (kg/m^3)
600	300	2.80964	6.88×10^{-7}	300.441	2.17×10^{-3}
600	150	5.41858	6.63×10^{-7}	300.589	1.08×10^{-3}
600	50	15.96370	6.49×10^{-7}	301.420	3.60×10^{-4}
450	300	2.08908	5.11×10^{-7}	300.627	2.16×10^{-3}
450	150	4.09733	5.01×10^{-7}	300.855	1.08×10^{-3}
450	50	12.04580	4.89×10^{-7}	301.859	3.59×10^{-4}
300	150	2.73491	3.34×10^{-7}	301.247	1.08×10^{-3}
300	50	8.06926	3.27×10^{-7}	302.491	3.58×10^{-4}

In order to estimate the thrust and make use of the available mass flow rate from the proposed feed system and plenum, the number of microchannels for the heater chip (the propulsion part) was calculated using the values presented by (Guerrieri *et al.*, 2015). In the (Guerrieri *et al.*, 2015) case, the heater chip consists of a grid with 67x67 circular microchannels were a single microchannel have $10^4\,\mu\mathrm{m}^2$ area and $500\,\mu\mathrm{m}$ length. For instance, using the condition where the plenum pressure is $300\,\mathrm{Pa}$ and the temperature of the chip is $573\,\mathrm{K}$, each microchannel employ a mass flow rate of

$5.75 \times 10^{-10}\,\mathrm{kg\,s^{-1}}$ generating a thrust of $500\,\mathrm{nN}$.

The *case 4* was chosen for comparison due to the stability of its properties along the domain and because it has an average sublimation pressure value, compared to the other simulated cases. In both cases the plenum pressure is at the same value of $300\,\mathrm{Pa}$. A mass flow of $5.11 \times 10^{-7}\,\mathrm{kg\,s^{-1}}$ would require 890 microchannels, corresponding approximately of a grid with 30x30 microchannels with the same cross-section area. With 890 microchannels the generated thrust is $0.445\,\mathrm{mN}$, and the specific impulse is maintained at $88.6\,\mathrm{s}$.

5. CONCLUSIONS

The propulsion concept described can overcome several *Cubesats* issues, such as strict safety requirements, useful lifetime, applicability and can work at a wider range of thrust. With the described methodology, predictions over the flow characteristics throughout the feed system and plenum were obtained for different inlet and outlet pressures. The tube is considered both as propellant tank and feed system, and operates below the water triple point, which ensures extremely low levels of thrust allowing more precise control. The results showed that it is possible to achieve a variation of mass flow in the plenum through variation of sublimation pressure and plenum pressure. This indicates that the LPM is able to operate under sublimation condition of the vapor water, varying the sublimation pressure for controlling the mass flow entering the plenum, and thus generate different levels of thrust.

Future investigations need to be carried out, such as assessing the presence of water vapor phase change throughout the feeding system and the plenum; the stability analysis, verifying the behavior of the system with greater numbers of mach; development of a mechanism to control the sublimation/evaporation in the tube. To this end, further in-depth analysis will be presented in future papers.

6. ACKNOWLEDGEMENTS

This present work was supported by FAPERJ, Carlos Chagas Filho Foundation for Research Support of Rio de Janeiro State. The authors would also sincerely like to thank CEFET-RJ for supporting the development of this research.

7. REFERENCES

Ahrens, J., Geveci, B. and Law, C., 2005. "Paraview: An end-user tool for large data visualization". *The visualization handbook*, Vol. 717.

Asakawa, J., Yaginuma, K., Tsuruda, Y., Koizumi, H., Nakagawa, Y., Kakihara, K., Yanagida, K., Aoyanagi, Y., Matsumoto, T., Matsushita, S. *et al.*, 2019. "Aqt-d: Demonstration of the water resistojet propulsion system by the iss-deployed cubesat". In *33rd annual AIAA/USU Conference on Small Satellite, SSC19-WKV-07, Logan, Utah*.

Bassoli, R., Granelli, F., Sacchi, C., Bonafini, S. and Fitzek, F.H., 2020. "Cubesat-based 5g cloud radio access networks: A novel paradigm for on-demand anytime/anywhere connectivity". *IEEE Vehicular Technology Magazine*, Vol. 15, No. 2, pp. 39–47.

CGEE, 2004. "Resumo executivo: Cubesats". Centro de Gestão e Estudos Estratégicos. 22 Apr. 2020 www.cgee.org.br/documents/10195/734063/CGEE_resumoexecutivo_CubeSats_Web.pdf.

Greenshields, C.J., 2015. "Openfoam user guide". *OpenFOAM Foundation Ltd, version*, Vol. 3, No. 1, p. 47.

Greenshields, C.J., Weller, H.G., Gasparini, L. and Reese, J.M., 2010. "Implementation of semi-discrete, non-staggered central schemes in a colocated, polyhedral, finite volume framework, for high-speed viscous flows". *International journal for numerical methods in fluids*, Vol. 63, No. 1, pp. 1–21.

Guerrieri, D.C., Silva, M.A., Cervone, A. and Gill, E., 2017. "Selection and characterization of green propellants for micro-resistojets". *Journal of Heat Transfer*, Vol. 139, No. 10.

Guerrieri, D.C., Silva, M.A., Cervone, A. and Gill, E., 2018c. "An analytical model for characterizing the thrust performance of a low-pressure micro-resistojet". *Acta Astronautica*, Vol. 152, pp. 719–726.

Guerrieri, D., 2018a. *The low-pressure micro-resistojet: Modelling and optimization for future nano-and pico-satellites*. Ph.D. thesis, Delft University of Technology.

Guerrieri, D., de Athayde Costa e Silva, M., Zandbergen, B. and Cervone, A., 2015. "Development of a low pressure free molecular micro-resistojet for cubesat applications". In *66th International Astronautical Congress, International Astronautical Federation, Jerusalem, Israel.* www.researchgate.net/publication/282148461_Development_of_a_Low_Pressure_Free_Molecular_Micro-Resistojet_for_Cubesat_Applications.

Guerrieri, D., e Silva, M.d.A.C., Cervone, A. and Gill, E., 2018b. "Optimum design of low-pressure micro-resistojet applied to nano-and pico-satellites".

Kang, S.J. and Oh, H.U., 2016. "On-orbit thermal design and validation of 1 u standardized cubesat of step cube lab". *International Journal of Aerospace Engineering*, Vol. 2016.

Karniadakis, G., Beskok, A. and Aluru, N., 2006. *Microflows and nanoflows: fundamentals and simulation*, Vol. 29. Springer Science & Business Media.

Kulu, E., 2020. "Nanosats database". Modern Language Association. 22 Apr. 2020 www.nanosats.eu.

Lee, R.H., Bauer, A., Killingsworth, M.D., Lilly, T., Duncan, J. and Ketsdever, A., 2008. "Free-molecule-microresistojet performance using water propellant for nanosatellite applications". *Journal of Spacecraft and Rockets*, Vol. 45, No. 2, pp. 264–269.

Lemmer, K., 2017. "Propulsion for cubesats". *Acta Astronautica*, Vol. 134, pp. 231–243.

Lemmon, E., McLinden, M., Friend, D., Linstrom, P. and Mallard, W., 2011. "Nist chemistry webbook, nist standard reference database number 69". *National Institute of Standards and Technology, Gaithersburg*.

Mehrparvar, A., Pignatelli, D., Carnahan, J., Munakat, R., Lan, W., Toorian, A., Hutputanasin, A. and Lee, S., 2014. "Cubesat design specification rev. 13". *The CubeSat Program, Cal Poly San Luis Obispo, US*, Vol. 1, No. 2.

NASA, 2017. "Cubesat 101: basic concepts and processes for first-time cubesat developers". *no. October*, p. 96.

Naseri, A., Pirayesh, R., Adcock, R.K., Stochaj, S.J., Shah, N. and Krizmanic, J., 2018. "Formation flying of a two-cubesat virtual telescope in a highly elliptical orbit". In *2018 SpaceOps Conference*. p. 2633.

Silva, M.d.A.C. *et al.*, 2018. *MEMS Micropropulsion: Design, Modeling and Control of Vaporizing Liquid Microthrusters*. Ph.D. thesis, Delft University of Technology.

Storck, W., Billett, O., Jambusaria, M., Sadhwani, A., Jammes, P. and Cutler, J., 2006. "A survey of micropropulsion for small satellites".

Trydal, J., 2015. *CFD analysis of temperature development due to flow restriction in pipeline*. Master's thesis, University of Stavanger, Norway.

Villela, T., Costa, C.A., Brandão, A.M., Bueno, F.T. and Leonardi, R., 2019. "Towards the thousandth cubesat: a statistical overview". *International Journal of Aerospace Engineering*, Vol. 2019.

Wagner, W., Saul, A. and Pruss, A., 1994. "International equations for the pressure along the melting and along the sublimation curve of ordinary water substance". *Journal of Physical and Chemical Reference Data*, Vol. 23, No. 3, pp. 515–527.

8. RESPONSIBILITY NOTICE

The author(s) is (are) solely responsible for the printed material included in this paper.